



Numerical simulation and experimental calibration of Additive Manufacturing by blown powder technology. Part I: thermal analysis

Journal:	<i>Rapid Prototyping Journal</i>
Manuscript ID	RPJ-10-2015-0136.R2
Manuscript Type:	Original Article
Keywords:	Additive Manufacturing (AM) process, Metal Deposition (MD) process, blown powder technology, Laser Solid Forming (LSF), FE modeling, thermo-mechanical analysis

SCHOLARONE™
Manuscripts

Numerical simulation and experimental calibration of Additive
Manufacturing by blown powder technology.
Part I: thermal analysis

KEYWORDS: Additive Manufacturing (AM) process, Metal Deposition (MD) process, blown powder technology, powder feeding, Laser Solid Forming (LSF), FE modeling, thermo-mechanical analysis.

Abstract

In this work, the numerical simulation of the Additive Manufacturing (AM) process known as blown powder technology is addressed. Specifically, Ti-6Al-4V metal powder is injected into the molten pool created by a focused high-energy laser beam and sintered according to the pre-specified scanning sequence. The result is a layer-by-layer metal deposition which can be used to build-up complex structures for components such as turbine blades, aircraft stiffeners, cooling systems, medical implants, among others.

The present Part I deals with the thermal analysis, while a subsequent Part II paper will target the mechanical stress analysis.

The numerical model proposed here adopts an apropos FE activation technology, which reproduces the same scanning pattern set for the numerical control system of the AM machine. This consists of a complex sequence of polylines, used to define the contour of the component, and hatch patterns to fill the inner section. The full scanning sequence is given through the Common Layer Interface (CLI) format, a standard input used for different manufacturing processes such as Rapid Prototyping (RP), Shape Metal Deposition (SMD) and machining processes.

The outcome of the proposed numerical model is calibrated with the experimental work carried out at SKLSP laboratories, where a Laser Solid Forming (LSF) machine, also referred to as Laser Engineered Net Shaping (LENS), is used to fabricate components by metal deposition.

The objectives of the present paper are three-fold: firstly, to calibrate the numerical formulation for the simulation of the AM process by blown powder technology, secondly, to show that a properly calibrated numerical model achieves high-fidelity reproduction of experimental results, and, thirdly, to investigate the sensitivity of the numerical model to both process parameters and thermo-physical material properties.

The thermal calibration of the computational model has direct impact in the subsequent stress and distortion analysis. Thermal deformations induced by the heating and cooling phases, as well as the shrinkage phenomena occurring during the sintering process of the powder material injected into the welding pool, are responsible for the possible quality defects of the fabricated component and the residual stresses induced by the manufacturing process. These aspects are studied in the Part II sequel of this work.

1 Introduction

Additive Manufacturing (AM), also known as 3D printing or Rapid Prototyping (RP), is a relatively novel technique to make parts, layer upon layer, directly from 3D model data. It is the opposite of subtractive manufacturing processes such as machining. 3D printing means that the fabrication makes use of print-heads or nozzles among other *printing* technologies.

This work focuses on the AM technologies for Metal Deposition (MD) by melting and sintering metal powders (e.g. titanium, Inconel, steel) making use of high-energy sources such as Electron Beam or laser.

The key benefit of the AM process is the freedom of design allowing for complex shapes, inner cavities impossible to produce by machining, very thin walls difficult to produce by casting, light weight parts with lattice/foam inner structures. The process flexibility allows for customized design in short production time where multiple pieces can be built as one without the need of complex tooling (e.g. moulds). Another advantage of this process consists of the rapid cooling of each deposited layer and, consequentially, a finer grain size compared to other metal forming technologies such as casting or forming.

A large number of products can be produced using AM technology: turbine blades, aircraft stiffeners, jet engine parts, microturbines, fuel injection swirlers are some examples in the aeronautical sector. Brackets, hydraulic manifolds, cooling systems, propellers, heat shields and different tooling inserts are also candidate products in the transport sector. Dental bridges as well as many different implants for the medical surgery and even a large variety of consumer goods can be also produced using this technology.

There are different AM processes using metal *powder* technology under rapid development. They can be classified in two main families:

1. *Powder bed technologies*. This is the case in Selective Laser Melting (SLM) or Selective Laser Sintering (SLS), where the metal powder is melted by a laser beam. Alternatively, in Electron Beam Melting (EBM) the metal powder is melted by an electron beam after a preheating step. Precision inkjet printing where the metal powder is mixed with a binder and after the printing operation, the part is consolidated by sintering. The main features of these technologies are the possibility of working with complex shapes, including small internal cavities thin walls, and a high-quality surface finishing.
2. *Blown powder or powder feeding technologies*, also known as Laser Metal Deposition or Laser cladding. In this process, the metal powder is blown coaxially to the laser beam which melts the particles on a substrate to form a metallurgical bond when cooled. Laser Engineered Net Shaping (LENS) or Laser Solid Forming (LSF) make use of this technology allowing for higher powder deposition rates compared to the powder bed technologies as well as the manufacturing of larger parts using coarser metal powders (Zhang et al 2009), (Tan et al 2010), (Tan et al 2010b) and (Huang et al 2014).

Many researchers have used the FE method to study additive manufacturing technologies, often taking advantage from the experience acquired in modeling welding processes (Aggarangsi et al 2003), (Labudovic et al 2003), (Jendrzejewski et al 2004), (Jendrzejewski et al 2007), (Zekovic

et al 2005), (Yang et al 2010), (Chiumenti et al 2010), (Anca et al 2011), (Marimuthu et al 2013), (Denlinger et al 2014), (Kelly et al 2014) and (Heigel et al 2015).

In this work, additive manufacturing (AM) by blown powder technology is addressed at two complementary levels: experimental and computational. The experimental work accurately portrays the manufacturing process in terms of both temperature and displacement evolution at different locations during the full duration of the AM process and the following cooling phase. The computational model is calibrated according to the experimental data. Thereafter, the resulting model may be used confidently to design more and more complex scanning patterns minimizing distortions, residual stress and hot-cracking risk.

The outline of the paper is as follows. The analytical and FE frameworks to deal with the analysis of the AM process are presented first. The description of the *activation* technique necessary to simulate the layer-by-layer metal deposition is detailed. The experimental work carried out at the *State Key Laboratory of Solidification Processing* (SKLSP) using a *LSF* machine is described next. The experimental setup and the thermal properties of the *Ti-6Al-4V* alloy are reported. Finally, the numerical results of the calibration and sensitivity analysis performed are shown.

2 Heat transfer analysis

Both the heating and the cooling phases of the AM process are controlled by the *balance of energy equation*. This can be stated as:

$$\dot{H} = -\nabla \cdot \mathbf{q} + \dot{Q} + \dot{D}_{mech} \quad (1)$$

where \dot{H} is the enthalpy rate (per unit of volume), \mathbf{q} is the heat flux, while \dot{Q} and \dot{D}_{mech} represent the heat source (per unit of volume) and the thermo-mechanical dissipation rate (per unit of volume), respectively.

For the AM process, the heat source is the energy input of the laser within the molten-pool formed along the scanning path and through the thickness of the substrate. The thermo-mechanical dissipation can be neglected in front of the power source of the laser beam.

The enthalpy $H(T, f_L)$ is a state variable defined as a function of the temperature, T , and the liquid fraction, f_L . Hence, the enthalpy rate in (1) results in:

$$\dot{H}(T, f_L) = \frac{\partial H}{\partial T} \dot{T} + \frac{\partial H}{\partial f_L} \dot{f}_L = C \dot{T} + L \dot{f}_L \quad (2)$$

where $C(T) = \frac{\partial H}{\partial T}$ is the (temperature dependent) heat capacity and $L = \frac{\partial H}{\partial f_L}$ is the latent heat released during the phase-change process.

The heat capacity is usually defined as: $C = \rho c$, the product of the material density, ρ , and the specific heat, c .

During the phase transformation the material volume, V , can be split into liquid and solid phases as: $V = V_L + V_S$. The liquid and solid fractions are defined as: $f_L = \frac{V_L}{V}$ and $f_S = \frac{V_S}{V}$, respectively, so that: $f_L + f_S = 1$. The evolution of the liquid fraction \dot{f}_L or, alternatively, $\dot{f}_S = -\dot{f}_L$ defines the phase change, that is, how the latent heat is absorbed or released during the transformation.

Remark 1 *The energy input induces the fusion of the material in the molten-pool followed by the solidification process which produces the coalescence of the metal powder on the substrate forming the new layer. The energy balance (accounting for the energy absorbed during the melting and the energy released during the solidification) is null and very localized in the Heat Affected Zone (HAZ).*

Remark 2 *The amount of latent heat is negligible in front of the energy input coming from the laser. Moreover, the HAZ is very narrow and the phase change occurs very quickly compared to the thermal diffusion process, so that its global effect is negligible in the heat transfer analysis.*

The heat flux (per unit of surface) \mathbf{q} , is computed as a function of the temperature gradient through the Fourier's law as:

$$\mathbf{q} = -k\nabla T \quad (3)$$

where $k(T)$ is the (temperature dependent) thermal conductivity. Due to the high conductivity of the metallic materials, the thermal diffusion process is the key mechanism of the metal deposition, driving the heat transfer in the manufacturing process.

Let V be an open and bounded domain in $\mathbb{R}^{n_{\text{dim}}}$ where n_{dim} is the number of dimensions of the space, closed by the smooth boundary $S = S_T \cup S_q$ where the corresponding boundary conditions are defined in terms of either prescribed temperature on S_T or prescribed heat flux on S_q . Suitable initial conditions for the transient thermal problem are defined in terms of initial temperature field: $T(t=0) = T_o$.

The resulting weak (integral) form of the energy balance equation (1), used for the heat transfer analysis, can be written as:

$$\int_V \left[(\rho c \dot{T} + L \dot{f}_L) \delta T \right] dV + \int_V [k \nabla T \cdot \nabla (\delta T)] dV = W_{ther}^{ext} \quad \forall \delta T \quad (4)$$

where δT are the variations of the temperature field, compatible with the Dirichlet boundary conditions (test functions), and W_{ther}^{ext} denotes the external work of the thermal loads:

$$W_{ther}^{ext}(\delta T) = \int_V \left[(\dot{D}_{mech} + \dot{Q}) \delta T \right] dV + \int_{S_q} [(\bar{q} + q_{cond} + q_{conv} + q_{rad}) \delta T] dS \quad (5)$$

The prescribed heat flux, \bar{q} , defined in (5), can be used to spread part of power input over the surface of the substrate.

The heat loss by convection, q_{conv} , can be taken into account using the Newton's law as:

$$q_{cond} = h_{conv}(T - T_{env}) \quad (6)$$

where $h_{conv}(T)$ is the (temperature dependent) Heat Transfer Coefficient (HTC) by convection, while T and T_{env} are the temperatures of material surface and the surrounding environment, respectively (see (Chiumenti et al 2008)).

Remark 3 *It is common to assume a constant value for the temperature of the surrounding environment, assuming that the process does not affect its value. This is not the case when the AM process is carried out in a closed chamber in a controlled atmosphere (e.g. argon to prevent the surface oxidation). The duration of the process is generally very long and a lot of energy is scattered in the chamber. The result is an increment of the environment temperature that cannot be neglected.*

Similarly, the heat flux due to the heat conduction process between the component and the clamping system, q_{cond} , can be computed as:

$$q_{cond} = h_{cond} (T - T_{clamp}) \quad (7)$$

where $h_{cond}(T)$ is the (temperature dependent) HTC by *conduction* between the two materials in contact, and T_{clamp} is the temperature of the clamping system.

Remark 4 *The HTC by conduction is defined as the inverse of the thermal resistivity between the two material in contact and it depends on different parameters defined at the contact interface such as the contact pressure and the surface roughness, among others. Considering contact between metallic materials, the value of the HTC is very high, around $1000 [W/m^2K]$. Hence, Newton's law can be replaced by prescribing the temperature at the corresponding contact surface, S_T as: $T = T_{clamp}$.*

Remark 5 T_{clamp} represents the temperature of the clamping system used to hold the substrate where the AM process takes place. Also in this case, its value cannot be assumed as constant in time if the thermal inertia of the substrate is comparable to the one of the clamping system (this was the case in our work). In fact, the high temperatures registered in the substrate are transmitted to the clamping system through the contact interface between them. This interface exhibits a very low thermal resistance to the heat flux when two metallic components are pressed together. Hence, the value of T_{clamp} should be known (or estimated) to avoid including the clamping system as part of the thermal analysis.

Finally, the radiation heat flux, q_{rad} , is the most important condition to dissipate the heat of the molten-pool and, more generally, at the HAZ, due to the high temperature field induced by the heat source. The radiation heat flux can be computed using Stefan–Boltzmann's law as:

$$q_{rad} = \sigma_{rad} \varepsilon_{rad} (T^4 - T_{env}^4) \quad (8)$$

where σ_{rad} is the Stefan–Boltzmann constant and ε_{rad} is the emissivity parameter, respectively.

Remark 6 *Stefan–Boltzmann's law can be rewritten as:*

$$q_{rad} = h_{rad} (T - T_{env}) \quad (9)$$

where $h_{rad}(T)$ is the (temperature dependent) HTC by radiation defined as:

$$h_{rad}(T) = \sigma_{rad} \varepsilon_{rad} (T^3 + T^2 T_{env} - T T_{env}^2 - T_{env}^3) \quad (10)$$

This format is interesting for two reasons: firstly, because it is possible to linearize the contribution of the heat radiation term as:

$$q_{rad} = h_{rad}(T^n) (T^{n+1} - T_{env}) \quad (11)$$

where $T^{n+1} = T(t^{n+1})$ is the current temperature at time t^{n+1} , and $T^n = T(t^n)$ is temperature in the previous time-step. The second reason is that it is extremely difficult to separate the heat

losses due to convection or radiation mechanisms. Hence, the numerical model can assume a unique HTC accounting for both heat convection and radiation terms, as:

$$q_{loss} = h_{loss}(T - T_{env}) \quad (12)$$

where $h_{loss}(T)$ is the (temperature dependent) HTC accounting for the total heat loss through the surrounding environment.

3 FE modeling of the AM process

The AM process is achieved by moving the heat source along a user-defined scanning pattern. Due to this localized heat input, sintering transforms the metal powder, injected into the molten-pool, into a new layer of material.

The numerical simulation of this procedure requires an *ad-hoc* procedure to apply the (volumetric) heat source (focussed on the substrate) to those elements *affected* by the moving energy input as well as to *activate* the elements forming the sintered layer (which is advancing following the powder deposition). Therefore, at each time-step of the simulation, a searching algorithm is used to identify the elements within the molten-pool as well as those representing the advancing metal deposition layer. This activation strategy, referred to as *born-dead-elements technique*, classifies the elements defined in the original finite element mesh into: active, inactive and activated elements. The *active* elements (e.g. the mesh which define the substrate) are computed and assembled into the global matrix. The *inactive* elements, such as the entire discretized domain where the scanning path is defined, are not included as part of the model: they have been generated but do not play any role in the computational model. At each time-step a number of elements (*activated* elements) are switched on according to the powder deposition along the scanning sequence defined by the user. Only active and activated elements are assembled into the solution model (see also (Chiumenti et al 2010)).

The advantage of this activation technique is the possibility of defining the computational mesh independently from the scanning-path. In particular, a structured FE mesh can be defined assuming a Cartesian grid discretization of the computational domain. This results in an easy and fast mesh generation which coincides, most of the time, with the movement of the heat source while filling the inner structures (hatch scanning) to obtain a solid model.

Remark 7 *The quiet elements technique is an alternative method. This considers that all the elements of the mesh defining the successive layers, which will be deposited during the process simulation, are included into the initial computational model. These elements are made passive (quiet) by setting material properties which do not affect the rest of the model (penalization). Very low values for both heat capacity and thermal conductivity are considered. Later on, following to the metal deposition process, the elements are activated, meaning that their real thermo-physical properties are re-established ((Heigel et al 2015)). This approach has different drawbacks: firstly, the simulation process is performed assembling all the elements and solving the full system of equations leading to a very high computational cost. Secondly, the penalization of the material properties of the passive elements induces an ill-conditioning of the solution matrix which may cause numerical problems for its solution such as a reduction of the convergence ratio of iterative solvers. Furthermore, when the focus is the stress analysis, fictitious strains are accumulated in the quiet elements*

and they will be transformed into spurious stresses when these elements are activated, spoiling the solution.

One of the added features of this work is the possibility of specifying the position of the laser source using the same input data as for the AM machine. The scanning-path is defined by a *Common Layer Interface* (CLI) format described in the following section. This is a great advantage, as it simplifies the end-user work by integrating the machine directives with the software interface. The scanning-path defines the sequence of points along the scanning trajectory and also the reference plane where the energy beam is focussed. It makes no reference either to the size of the molten-pool or to the thickness of the deposited layer. The cross-section of the layer deposited, that is, its thickness and width, as well as the spot-size of the laser beam must be specified separately to define completely the simulation process.

Remark 8 *The objective of the present work is the analysis of the AM process at global level (component scale) where the size of the layer section is assumed as known. The study of the process at local level (molten-pool analysis) is out of the scope of this work. The local level approach is used to characterize the relationship among the different process parameters affecting the powder sintering process as: the energy input affecting the temperature of the molten-pool and the surrounding HAZ (see (Wei et al 2012) and (Wei et al 2015)), the laser-spot size, the scanning speed, the powder feeding, etc.*

From the numerical point of view, the implications derived from the space discretization (FE mesh adopted) and the time-stepping defined for the time-integration of the thermal (transient) problem must be considered.

A first consideration regards the discretization in time. The discrete problem is characterized by a time-step, $\Delta t = t^{n+1} - t^n$, so that a discrete sequence of computations is performed according to the time-marching scheme. Therefore, the molten-pool does not continuously move along the scanning path (as for the continuous problem) but, instead, it is *stepping* from its position at time t^n to that at time t^{n+1} . Consequently, the power input is intermittent along the scanning path, producing a discontinuous HAZ. The problem can be alleviated by reducing the time-step, to get an overlapped molten-pool progression, but not completely avoided.

Alternatively, the total power input delivered within the time-step, Δt , can be distributed to the elements belonging to the volume affected by the power input during this interval, which has at both ends the molten-pools at times t^n and t^{n+1} . As a result, the molten-pool is defined by a rectangular section $v_{MD}\Delta t$ long (being v_{MD} the scanning-speed) and r_{pool} wide (as the laser-spot size), which penetrates h_{pool} in depth within the substrate. At the same time, a new layer of material is added above it due to the coalescence process of the metal powder deposited. This layer is defined by its average thickness and width: t_{MD} and b_{MD} , respectively.

A second consideration is about the space discretization. Even if the HAZ is discretized using a very fine mesh, it is very challenging to achieve enough spatial resolution to define exactly the ideal volume where the power input must be delivered.

Remark 9 *In the literature it is possible to find different models to represent the heat source with different degrees of sophistication. The double ellipsoidal power density distribution illustrated by*

Goldak et al. ((Goldak et al 1984)) is the base of many models proposed for its accurate characterization (e.g. (Rosenthal 1941), (Tian et al 2008), (Gajapathi et al 2011), (Rahman et al 2014) and (Lacki et al 2011)). This is mandatory, when the focus is the local-level analysis to study the thermal convection within the molten-pool. Nevertheless, at global-level, it is much more important to account for the right amount of energy introduced into the HAZ, more than its local density distribution.

According to the outcome of the searching algorithm, it is possible to sum the volume of all the elements belonging to the (discretized) molten-pool as:

$$V^{pool} = \sum_{e=1}^{ne} V^{(e)} \Big|_{e \in pool} \quad (13)$$

so that the (average) density distribution of the heat source (per unit of volume) is computed as:

$$\dot{Q} = \frac{\eta \dot{P}}{V^{pool}} \quad (14)$$

where \dot{P} is the total energy input and η the actual heat absorption efficiency. This power re-distribution preserves the total energy input independently of the mesh used (see (Chiumenti et al 2010)).

The balance of energy equation in (4) establishes the equilibrium between the energy input and the heat loss. The same care devoted to estimate the energy delivered by laser beam and absorbed by the substrate must be placed to compute the heat dissipated through the boundaries of the AM domain. This domain is also changing due to the AM process, requiring a specific searching strategy to update the contour surface at each time-step of the numerical simulation. Following the activation process, this updating is necessary to compute the current size of the boundary surfaces subjected to the heat radiation and heat convection fluxes, and, consequently, perform an accurate heat transfer analysis of the AM process.

4 CLI-format to define the scanning-path

The Common Layer Interface (CLI) is a universal format for the input of geometry data to model fabrication systems based on layer manufacturing technologies (LMT). It is intended as a simple, efficient and unambiguous format independent of vendors or fabrication machines. The flexibility of the CLI format allows for its use in a wide range of applications such as systems using layer-wise photo-curing of resin (e.g. additive layer manufacturing processes for rapid prototyping), sintering of powder materials (e.g. metal deposition processes using LENS or SLM technologies), cutting and machining processes, solidification of molten materials, medical scanners, and other systems which build models on a layer-by-layer basis.

The 3D-model is sliced with parallel planes and the volume between two slices is a layer. Hence, the geometrical model is defined by the sum of all the layers. The slicing plane is parallel to the xy -plane and it is assumed that the building direction is the positive z -axis.

Each layer is defined by its thickness and a set of contours and hatches. *Contours* represent the boundaries of the solid model within a layer, and are defined by polylines. Each polyline is

defined by a set of point coordinates (x, y) , connected contiguously in the listed order by straight line segments. A *hatch* is a set of independent straight lines, each defined by one start and one end point. The purpose of hatches is to define filling structures to obtain the solid model.

An example of CLI file in ASCII-format is presented in Table 1.

\$\$HEADERSTART	// This is an example of CLI-format //
\$\$ASCII	// File is in ASCII-format //
\$\$UNITS/1	// Coordinates are given in [mm]//
\$\$DATE/110715	// 11 July 2015 //
\$LAYERS/100	// Geometry made of 100 layers //
\$\$HEADEREND	
\$\$GEOMETRYSTART	// Start of GEOMETRY-section//
\$\$LAYER/2.5	// Layer entry level at $z = 2.5$ [mm] //
\$\$POLYLINE/1 1 3 8.5 9.2 2.1 9.3 3.2 2.6	// 3 points (x, y) defining the polyline //
\$\$HATCHES/1 1 7.5 9.2 2.7 9.2	// 2 points (x, y) defining the hatch line //
...	

Table 1: Example of a CLI file in ASCII-format to define the scanning-path sequence.

Both polylines and hatches are defined by coordinates of points. No reference to the time-scale is mentioned. Typically, the movement of the laser-head is defined by two parameters: the scanning-speed, v_{MD} , when the laser is switched-on, and the back-speed, v_{back} , when the laser is switched-off and it is repositioning. Hence, an automatic time-stepping Δt_{on} is defined by splitting each polyline (and hatch) segment according to a fix advancing step Δs of the laser-head predefined by the end-user as a function of the dimensions of the solid model. When the laser is switched-off, the time-increment Δt_{off} is computed as a function of the back-speed and the distance Δx between the coordinates of the last scanning point (end of polyline or hatch) and the beginning of the following one:

$$\begin{aligned} \Delta t_{on} &= \Delta s / v_{MD} && \text{During the laser scanning} \\ \Delta t_{off} &= \Delta x / v_{back} && \text{For repositioning} \end{aligned} \quad (15)$$

Remark 10 *It is important to include the repositioning interval Δt_{off} as part of the thermal analysis because of the the fast cooling experienced by the material during its duration.*

5 Experimental work

The experimental work has been carried out at the *State Key Laboratory of Solidification Processing (SKLSP)* using the laser solid forming (*LSF-III*) machine shown in Figure 1a. The system uses a CO_2 -laser source with a maximum power input of 4 [kW] in a closed chamber with a protective atmosphere (argon) to prevent oxidation. Figure 1b shows the coaxial nozzle used for the powder blowing. Its movement is monitored by a numerical control device. Temperature is measured using *OMEGA GG-K-30* thermocouples and a midi *LOGGER G900-4/8* data recorder.

The substrate samples consist of *Ti6Al4V* Titanium alloy plates, 140 [mm] long, 50 [mm] wide and 6 [mm] thick. Each plate is burnished by sand paper and cleaned using anhydrous-alcohol

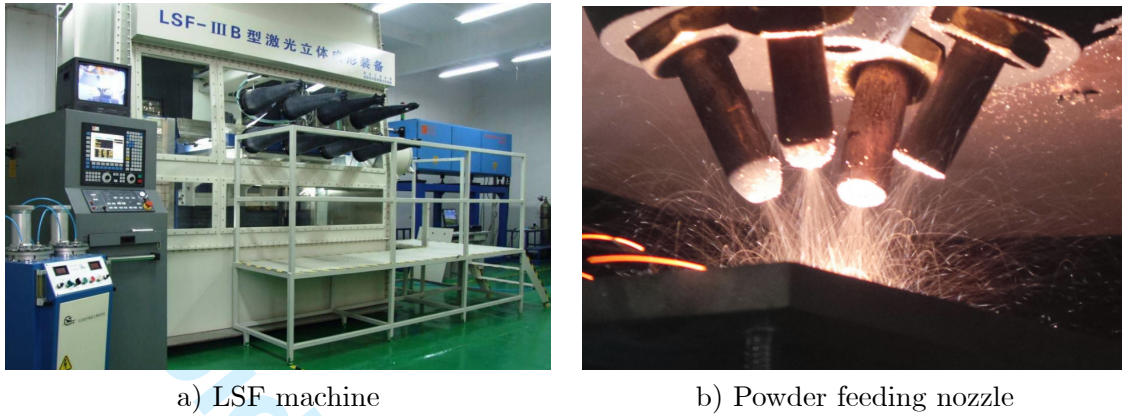


Figure 1: Experimental facilities at SKLSP.

and acetone. After this, 5 thermocouples are spot-welded: 3 on the lower surface and 2 more on the upper surface of the sample as shown in Figures 3a-b. Finally, the substrate is clamped to the supporting system and anchored inside the chamber of the AM machine. The $Ti6Al4V$ powder is dried in a vacuum oven at $120 [^{\circ}C]$ before supplying it to the feeding device. Figure 2a shows the preparation of one of the substrates as well as the supporting system to be introduced inside the chamber of the *LSF* machine. The final metal deposition is presented in Figure 2b.

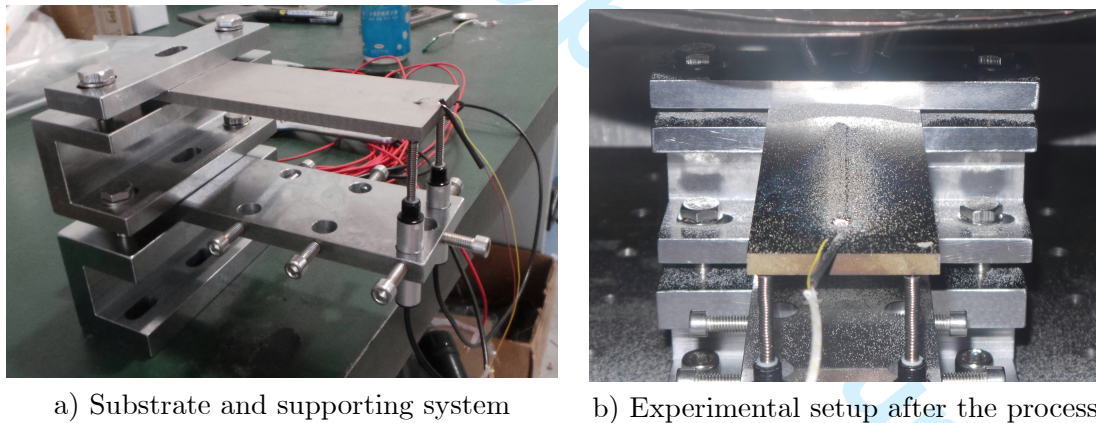


Figure 2: Substrate plate and supporting system used for the AM process.

Table 2 shows the parameters used to inform the control system of *LSF* machine.

The scanning path is shown in Figure 3c. This sequence is repeated 10 times to build 10 layers of added material. The up-lift of the nozzle is $0.3 [mm]$ assuming that this is the incremental height of each layer for a final metal deposition $3 [mm]$ high (approx.).

Power input	2	[kW]
Laser beam size	1.6	[mm]
Offset distance	0.8	[mm]
Up-lift height	0.3	[mm]
Scanning speed	10	[mm/s]
Back speed	50	[mm/s]
Powder feeding	8.5	[r/min]

Table 2: Process parameters used to inform the LSF machine.

6 **Material characterization**

The numerical simulation of the AM process requires the characterization of the thermo-physical properties of the material. Their values are temperature dependent, covering the full range from room temperature to fusion temperature.

Figure 4 shows the temperature-dependent properties for the *Ti6Al4V* titanium alloy, used for both the substrate and the powder feeding ((Bermingham et al 2007) and (Elmer et al 2004)).

The liquidus-to-solidus phase change is defined by a latent heat of $L = 290 \text{ [kJ/kg]}$, together with the liquidus and solidus temperatures of $1703 \text{ [}^\circ\text{C]}$ and $1697 \text{ [}^\circ\text{C]}$, respectively.

The substrate is clamped to a supporting structure made of stainless steel. This structure is not analyzed, even if its thermal inertia influences the temperature evolution at the contact interface with the substrate, that is, the heat loss by heat conduction through the clamping system.

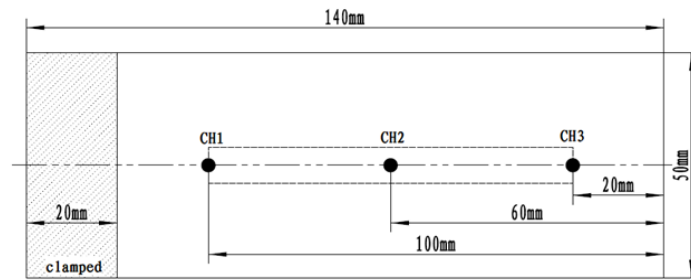
7 **Numerical results**

This section describes the calibration of the in-house COupled MEchanical-Thermal FE software *COMET* customized for the numerical simulation of the AM process (Cervera et al. 2002). Computations and CPU-times refer to a laptop equipped with an *i5* Intel processor.

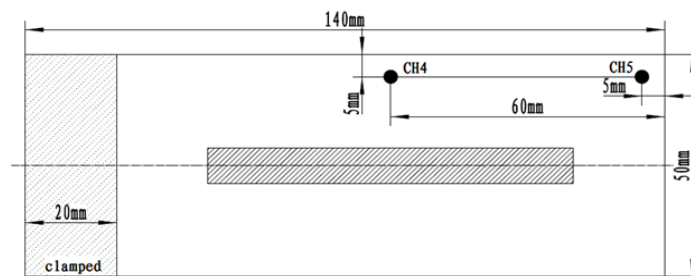
The results obtained from the numerical simulation are presented in terms of temperature graphs at the different thermocouple locations on the substrate, as well as temperature contour-fills, using the in-house pre-post-processor *GiD* (<http://www.gidhome.com>). These results are compared with the corresponding measurements obtained at *SKLSP* research labs.

7.1 **Calibration and sensitivity analysis**

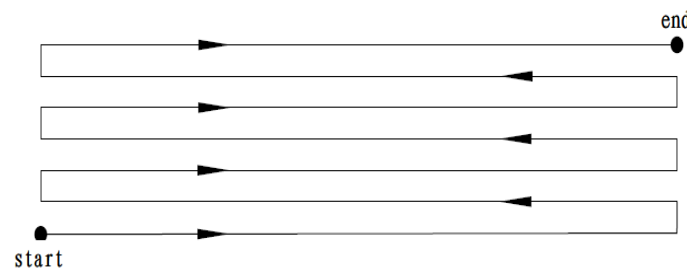
The calibration and sensitivity analysis have been carried out using the *FE* discretization shown in Figure 5a. It consists of 12,456 nodes and 10,050 hexahedral elements. The average mesh size is 2.5 [mm] , with 5 elements placed through the thickness of the plate. A finer mesh, with average element size of 0.875 [mm] , is used at the process zone to be able to capture both the high temperature gradient induced by the AM process and the scanning pattern used for the metal deposition (see Figure 5b). The mesh size adopted for the metal deposition closely approximates the actual dimensions of the sintered titanium powder: 80 [mm] long, 7 [mm] wide (6.4 [mm] expected) and 2.8 [mm] thick (3 [mm] expected). Hence, the average layer thickness is set to 0.28 [mm] while the spot-size is set to 1.75 [mm] with 50% overlapping during the scanning operation.



a) Lower surface



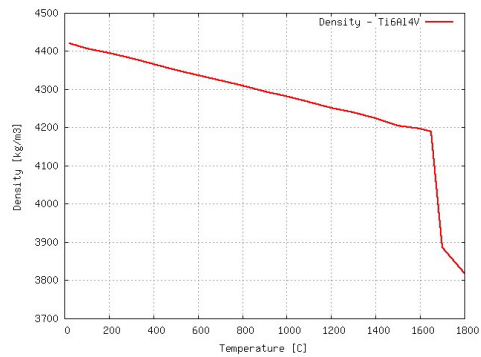
b) Upper surface



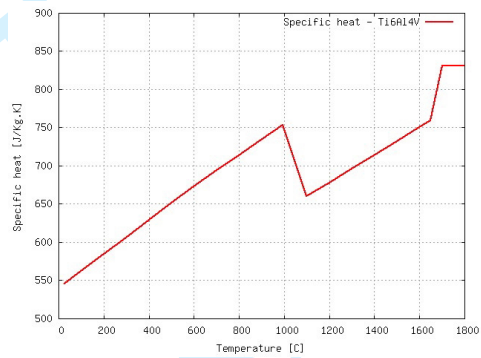
c) Scanning sequence

Figure 3: Location of the thermocouples on the (a) lower and (b) upper surfaces of the substrate; (c) Scanning sequence

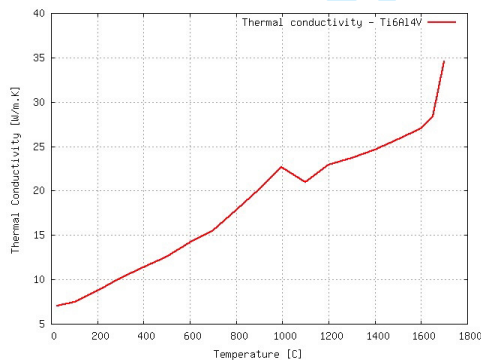
Note that even if the expected and the actual dimensions of the metal deposition are not very different (less than 10%), their correct values are necessary not to over-estimate the thermal inertia of the sintering material.



a) Density



b) Specific heat



c) Thermal conductivity

Figure 4: Ti6Al4V titanium alloy: thermal properties.

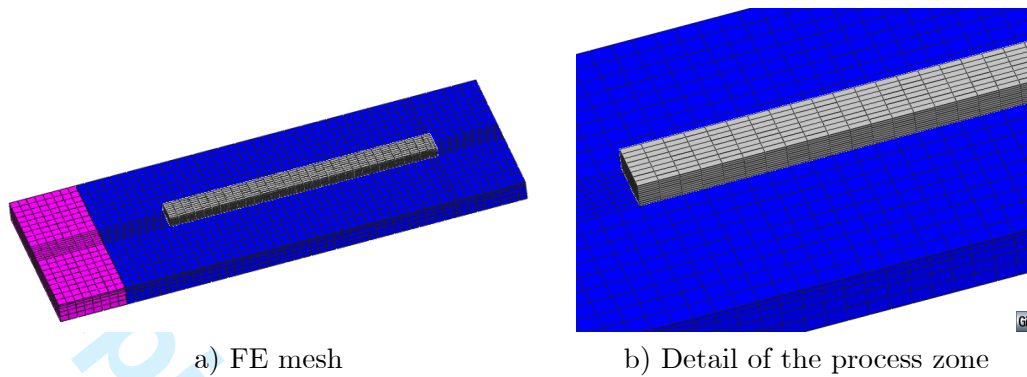


Figure 5: FE mesh used for the numerical simulation of the AM process.

The colored zone in Figure 5a represents the surface in contact with the clamping system used to restrain the movement of the substrate plate. Conduction heat transfer at the contact interface between the plate and the clamping system is considered. The heat transfer coefficient used for Newton's model is $50 \text{ [W/m}^2\text{K]}$. The temperature of the supporting structure is often assumed as constant during the analysis because its thermal inertia is generally much higher than the one of the sample. This was not the case in the experimental setting, so that the temperature of the clamping surface was monitored during the entire duration of the AM process and the following cooling phase. Figure 6b shows the temperature evolution at the clamping system as well as the approximating curve used for the numerical simulation.

The AM process is performed in a closed chamber with a protective atmosphere to prevent oxidation. Also in this case, the environment temperature was not constant. Figure 6a shows the actual temperature evolution inside the chamber. Unfortunately, the thermocouple was placed too close to the process area being affected by the heat radiation during AM process. The (conservative) environment temperature value used for both radiation and convection models is shown in Figure 6a (blue line). The HTC coefficient used for the heat convection model is $10 \text{ [W/m}^2\text{K]}$ while emissivity coefficient used for the heat radiation model is 0.7.

Table 3 shows the process parameters used for the numerical simulation. These parameters are slightly different from those in Table 2, according to the actual measurements of the metal deposition.

Figures 7a-b show both measured and calculated temperatures at the lower and upper surfaces, respectively. The level of agreement is remarkable. A closer view is presented in Figures 7c-d where it is possible to appreciate the accuracy of the numerical results.

Remark 11 *Thermocouples 4 and 5, placed on the upper surface of the substrate, were shielded to protect against radiation. Nevertheless, the recorded temperatures still suffer by the heat radiation effects.*

The simulation strategy consists of 3 phases: the pre-heating phase, the AM phase and, finally, the cooling phase. During the simulation of the manufacturing phase, the power absorption is

Power	2	[kW]
Power absorption	16.5	[%]
Scanning speed	10	[mm/s]
Back speed	50	[mm/s]
Penetration	0.28	[mm]
Layer thickness	0.28	[mm]
Layer width	1.75	[mm]
Overlapping	50	[%]

Table 3: Process parameters used for the numerical simulation.

set to 16.5% meaning that most of the energy input is scattered in the surrounding environment, in agreement with the experimental experience at *SKLSP*. Figures 8a-b show the sensitivity to the power absorption parameter. This is the most important parameter of the balance of energy equation in (4) defining the energy input into the system. During the pre-heating phase, the absorption parameter is reduced up to 10%. This phase is not contemplated in the experimental setting, but it can be clearly observed that the powder sintering is much less during the scanning sequence defined for first layer. This is due to the low temperature of the substrate in this first phase and it can also explain the mismatch (0.2 [mm] approx.) between the estimated and the actual height of the metal deposition.

Figure 9a and the corresponding detailed view in Figure 9b shows the temperature evolution at thermocouple 2 and its sensitivity to the pre-heating phase.

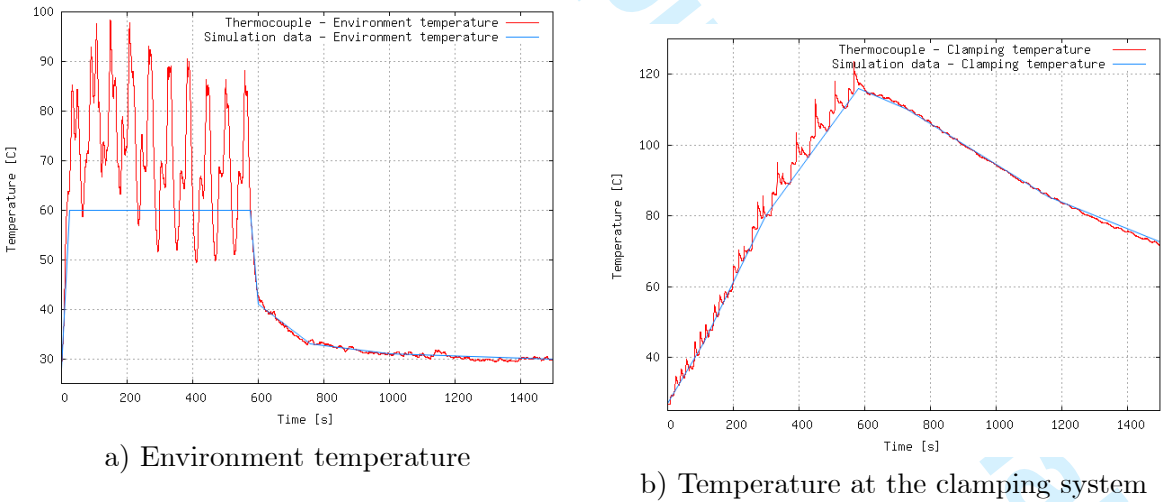
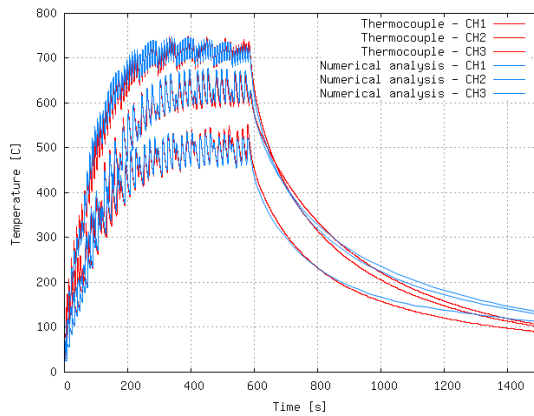
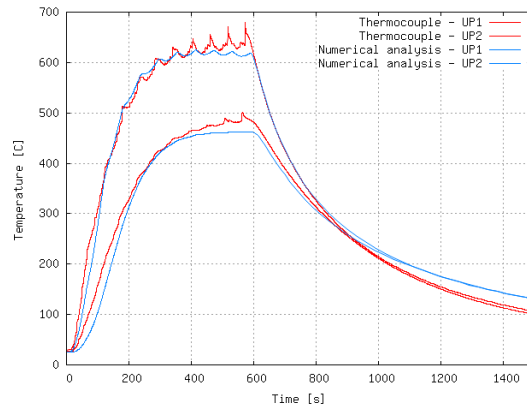


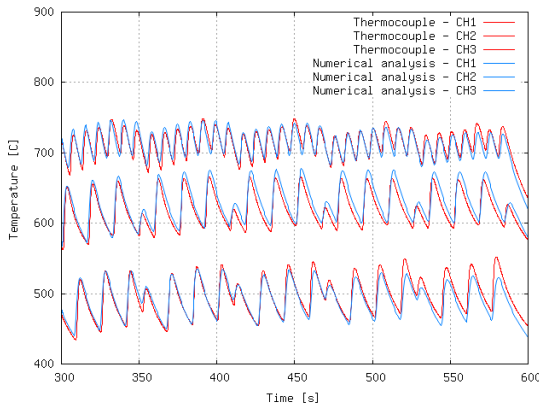
Figure 6: Actual temperature of the environment (inside the AM chamber) and at the clamping system. Measured values and simplified evolution for the numerical model.



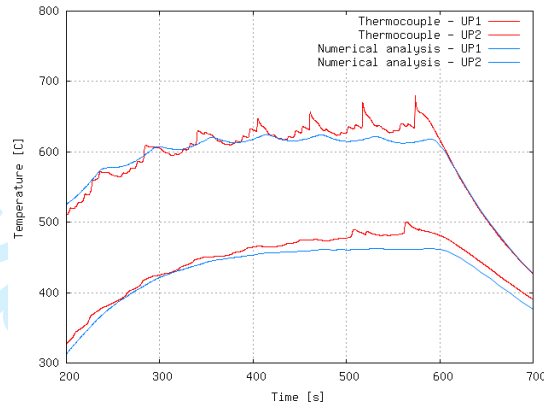
a) Thermocouples placed on the lower surface of the substrate



b) Thermocouples placed on the upper surface of the substrate



c) Detail of thermocouples placed on the lower surface of the substrate



c) Detail of thermocouples placed on the upper surface of the substrate

Figure 7: Temperature evolution at 5 thermocouple locations: 3 placed on the lower surface of the substrate (CH1, CH2 and CH3) and 2 on the upper surface (CH4 and CH5). Comparison between the experimental evidence and the numerical model.

Remark 12 *The benchmark proposed for the calibration of the numerical model only considers 10 layers of metal deposition, highlighting the difference between the pre-heating and the manufacturing phases. In the case of much higher depositions, the pre-heating phase can be neglected.*

During the AM process both the substrate (at the melting pool) and the powder material undergo the phase change: the energy input generates the molten pool and melts the blown powder. The material is sintered, forming a new layer by the coalescence process. Both the heating and the cooling phases are very fast and, the latent heat is firstly absorbed (melting phase) and later,

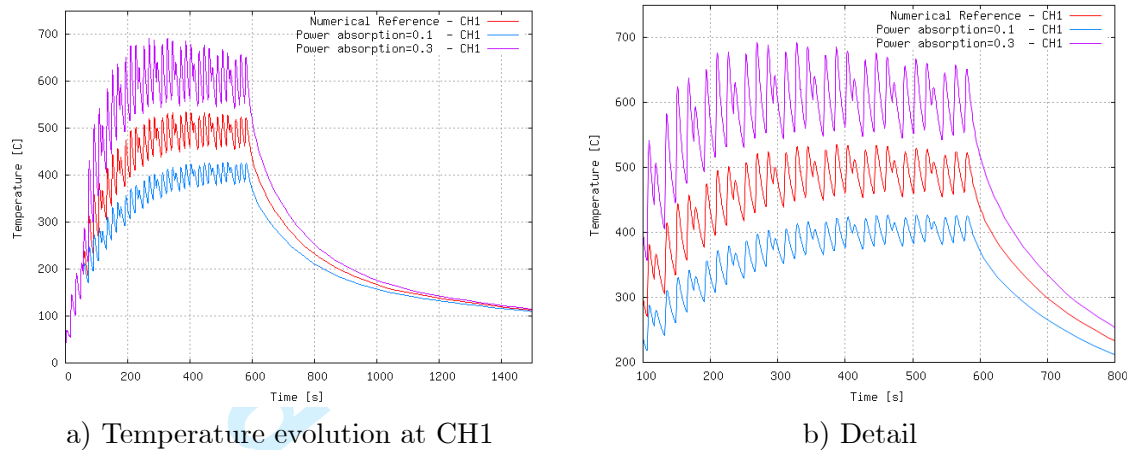


Figure 8: Sensitivity to the power absorption parameter.

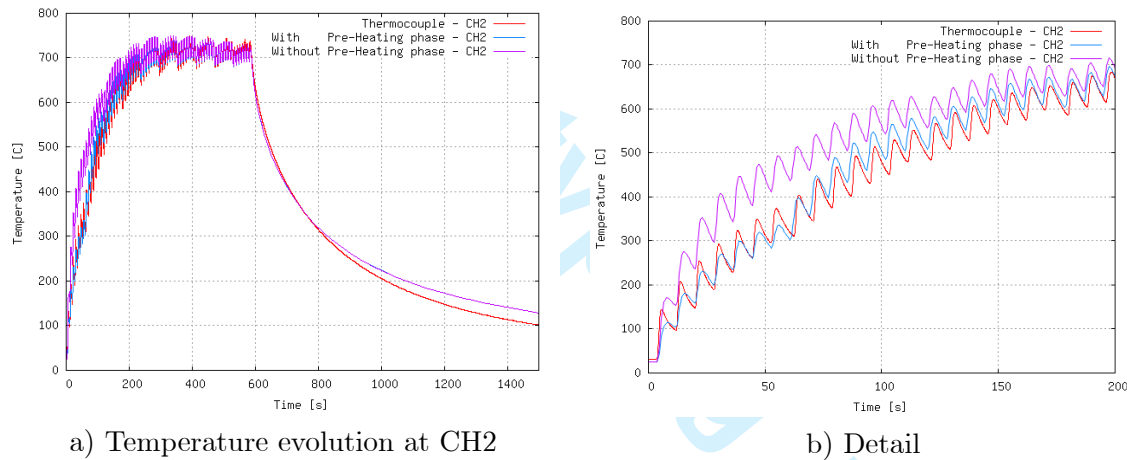


Figure 9: Effect of the pre-heating phase. Comparison between the measured temperature evolution at thermocouple CH2 and the numerical simulation.

is released (sintering phase). Hence, the effect of the latent heat contribution at *global* level is negligible as shown in Figures 10a-b. All the curves are perfectly overlapping. This result is remarkable because, without considering the phase-change, the CPU-time is reduced by 3 times (1 iteration per time step instead of 3-4 during the phase-change) making much more affordable the numerical simulation of the AM process. Table 5 shows the CPU-time of the first simulation proposed (used as reference) and the case where the phase-change is not considered.

The sensitivity to the heat loss models is presented next. This is a key point when studying the AM simulation process. The equilibrium between the energy absorption and the heat dissipation

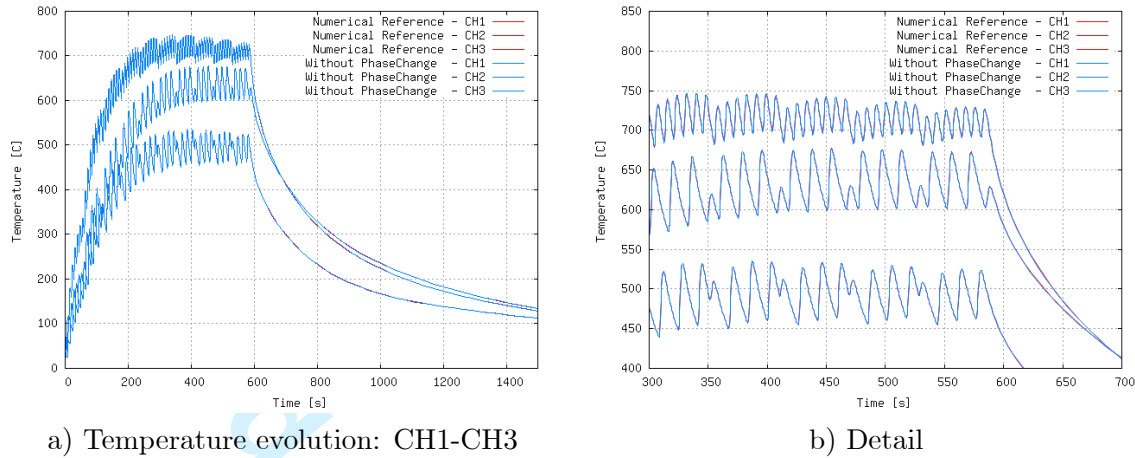


Figure 10: Effect of phase-change latent heat contribution.

through the surrounding environment defines the temperature evolution in the manufactured component. To uncouple the two mechanisms, the heat loss has been calibrated analyzing the cooling phase, when the energy input is switched-off. From the physical point of view, both heat convection and heat radiation coexist but it is difficult to split their effects. In this work, the reference solution is obtained by calibrating the heat radiation model, while keeping the HTC of the convection model (h_{cond}) to a constant value of 10 [W/m^2K]. The resulting emissivity coefficient used for the heat radiation model was: $\varepsilon_{rad} = 0.7$.

Figure 11a shows the response of the numerical model when using the heat convection model, only. The result is incorrect from both the quantitative and qualitative points of view, both in the cooling and heating phases. In fact, even if the HTC is increased (or the power absorption is reduced) to capture the maximum temperature level, the temperature evolution is still far from the experimental evidence. More specifically, the cooling phase is always too slow, while the heating phase never shows the temperature saturation exhibited by the material, as shown in Figure 11b. Figure 11c presents the temperature evolution at the thermocouple 2, when the heat radiation

Temperature [$^{\circ}C$]	HTC [W/m^2K]
20	6
200	10
400	20
600	40
800	70
1000	110
1200	160

Table 4: Best suited HTC for the convection model.

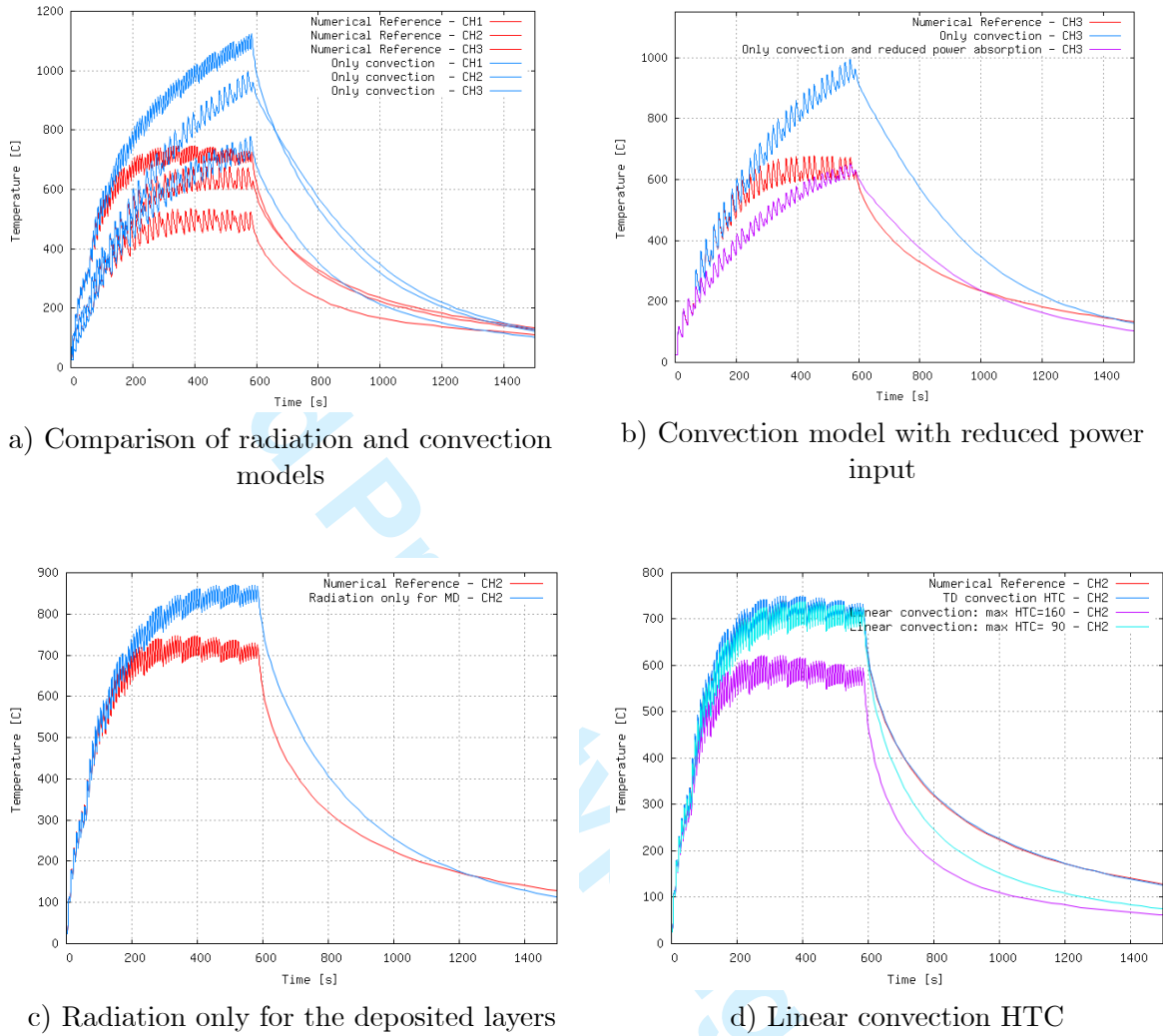


Figure 11: Effect of the heat loss by radiation. Comparison between radiation and convection models.

model is used for the metal deposition layers, only. Once again, is demonstrated that the main mechanism to dissipate the heat from the substrate is by radiation ((Heigel et al 2015)). Table 4 shows the values of $h_{loss}(T)$ when using a temperature-dependent HTC for the total heat loss as presented in Eq. (12). This model (not shown) gives exactly the same solution as the numerical reference.

Finally, the response of the numerical model, when a simpler linear interpolation of the HTC between $20^{\circ}C$ and $1200^{\circ}C$, is presented in Figure 11d. If a maximum value of $160 [W/m^2K]$ is adopted as in Table 4, the temperature curves reaching too low values. Instead, when using $90 [W/m^2K]$ as top value, the response compares better with the reference one.

Figure 12a shows the sensitivity of the model to the temperature of the surrounding environment. The difference is negligible when the radiation model is used, while a small mismatch can be observed when only the convection model is adopted, as shown in Figure 12b.

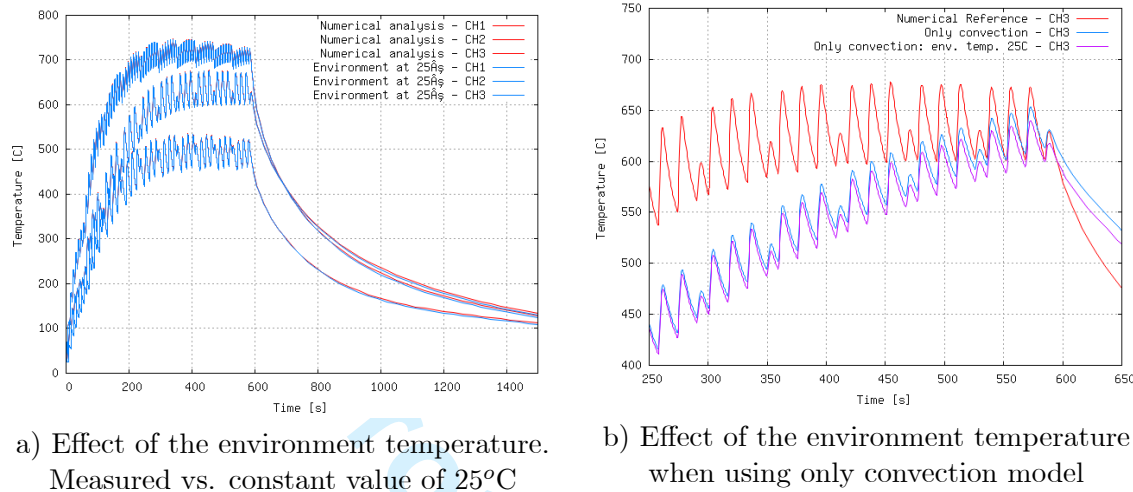


Figure 12: Effect of the actual temperature of the environment (measured inside the AM chamber) on the response of both radiation and convection models.

The most suitable heat loss mechanism at the contact interface between the substrate and the clamping system is by heat conduction, using the Newton's law presented in Eq. (7). Also in this case, the HTC as well as the temperature of the clamping system must be defined. In Figure 13a is demonstrated that the differences due to the temperature defined at the clamping interface is almost negligible during the heating phase. An appreciable discrepancy is shown during the cooling phase. Using a constant value of 25°C, the final equilibrium temperature is lower than expected because of the heating of the supporting structure. More important, is the definition of the HTC by conduction: this is the inverse of the thermal resistivity at the contact interface. Its value depends on the roughness of the surfaces in contact as well as on the contact pressure established. In our case, the most suitable value was 50 [W/m²K] being far from the typical value of 1000 [W/m²K] when the contact is almost perfect. This can be explained by the fact that the bolts' torque was very low because it was applied manually. Figure 13b shows the model sensitivity to the HTC value, comparing with the calibrated numerical reference.

Finally, some considerations about the time-stepping used are necessary. The calibrated solution makes use of an automatic time-step which moves the heat source element-by-element (Courant's number: $Cu = 1$). This hypothesis allows for the most accurate and more CPU-time consuming result. The time-step can be increased while reducing the simulation accuracy. One interesting option is to study the response of the numerical model when all the elements belonging to one scanning hatch are simultaneously activated. This means 7 time-steps, and the corresponding cooling intervals after the activation of each hatch, for each deposited layer. The result is presented in Figures 14a-b. It is interesting to observe that, even if the hatch-by-hatch activation loses the

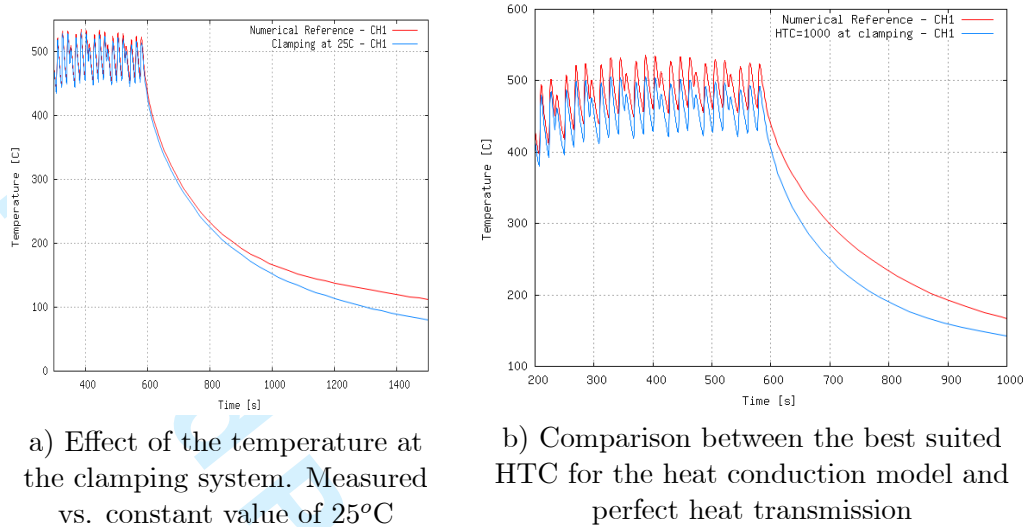


Figure 13: Effect of the HTC and the actual temperature measured at the clamping system used for the heat conduction model at the contact interface between the substrate and the supporting structure.

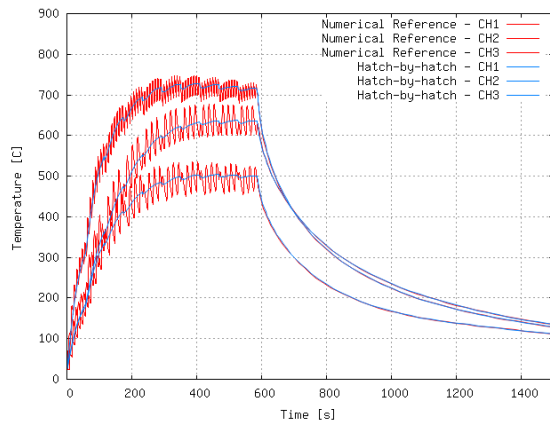
oscillatory response of the temperature, it conserves its average value. Also, the activation sequence could be performed in a layer-by-layer manner. In each time-step, all the elements belonging to one layer are activated adopting an *equivalent* scanning speed of 1.4 [mm/s]. The result is presented in Figures 15a-b. Once again, the balance of energy allows for an average estimation of the temperature profiles while losing all the details concerning the scanning sequence.

Clearly, the advantage of these simplified strategies is in the CPU-time which is notably reduced as show in Table 5.

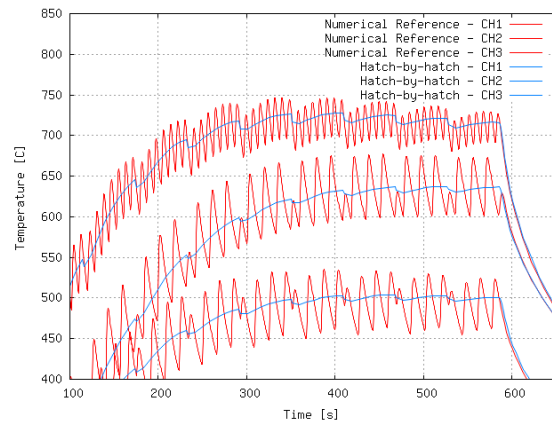
Strategy	CPU-time [s]	[%]
Reference	1356	100
No phase-change	473	35
Hatch-by-hatch	61	4
Layer-by-layer	29	2

Table 5: Simulation CPU-time using different strategies.

Remark 13 Even if the hatch-by-hatch and the layer-by-layer activation sequences may appear promising because of the CPU-time reduction, the mechanical response can be compromised when performing the stress analysis. In fact, the final microstructure, the mechanical properties, the plastic deformations and the residual stresses are influenced by the complex thermal history (local heating and cooling) induced by the scanning pattern.

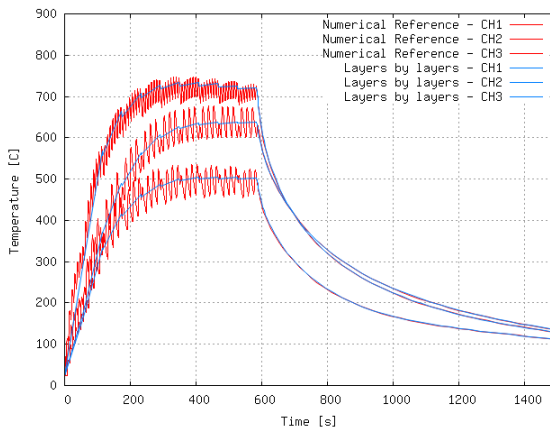


a) Temperature evolution at lower thermocouple locations

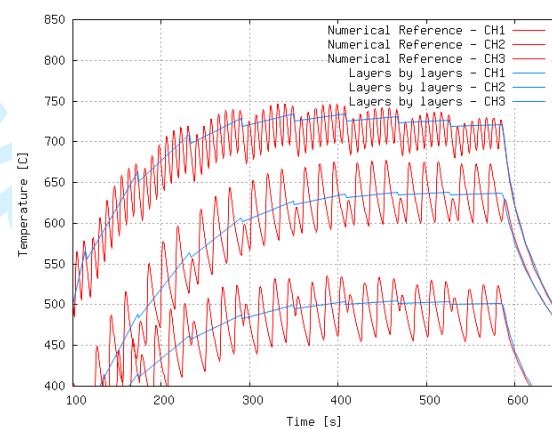


b) Detail of temperature evolution at lower thermocouple locations

Figure 14: Metal deposition built-up hatch-by-hatch. 7 hatches for each layer.



a) Temperature evolution at lower thermocouple locations



b) Detail of temperature evolution at lower thermocouple locations

Figure 15: Metal deposition built-up layer-by-layer. One time-step for each layer.

Figure 16a shows the sample after cooling at room temperature with the mark induced by the red-hot temperature field. Figure 16b shows the temperature contour-fill at the end of the AM process just before cooling. Once again the agreement is remarkable.

8 Conclusions

In this work, a FE framework for the numerical simulation of the AM process is presented detailing the mechanisms of energy absorption and heat dissipation through the surrounding environment. The apropos FE activation technique is also discussed, focussing on the numerical simulation of fabrication processes by blown powder technology.

The experimental work has been carried out at SKLSP laboratories using a Laser Solid Forming (*LSF-III*) machine.

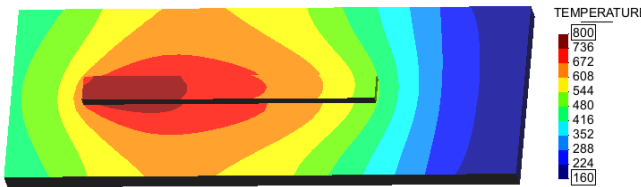
The calibration of the numerical model has demonstrated a remarkable agreement with the experimental evidence both during the deposition process and the following cooling phase to the room temperature.

This work has also studied the sensitivity to different process parameters as well as thermo-physical properties. The outcome is the following:

- The model is very sensitive to the energy absorption parameter. In the case of blown powder technology, this parameter can be adjusted around 15%. A slightly lower value (10%) can be considered during the scanning of the first layer (pre-heating phase) because of the colder temperature of the substrate at the beginning of the fabrication process.
- Heat radiation is the main mechanism to dissipate the heat through the surrounding environment. It cannot be neglected, but it could be replaced by a temperature-dependent HTC. The temperature variation inside the process chamber or at the clamping system can be neglected, even if a better accuracy can be achieved in the cooling phase when those data are available.
- The latent heat contribution of the liquidus-to-solidus phase-change can be avoided, saving 60% of the total CPU-time. Its effect at global level is negligible.



a) Oxidation observed after AM process



b) Temperature contour-fill at the end of the AM process

Figure 16: Temperature contour-fill at the end of the manufacturing process. Comparison with the residual sample mark.

- The simulation time can be speed-up by considering a hatch-by-hatch or either a layer-by-layer deposition sequence. Average temperature fields can be recovered but the accuracy of the local thermal history is lost.

The thermal calibration of the computational model has direct impact in the subsequent stress and distortion analysis. Thermal deformations induced by the heating and cooling phases, as well as the shrinkage phenomena occurring during the sintering process of the powder material injected into the molten pool, are responsible for the possible quality defects of the fabricated component and the residual stresses induced by the manufacturing process. These aspects are studied in the Part II sequel of this work.

9 Acknowledgments

Financial support from the European Commission - Factories of the Future (FoF) Programme under the *CAxMan* Project – *Computer Aided Technologies for Additive Manufacturing* and the MG-2015 SingleStage-A Programme under the *EMUSIC* project – Efficient Manufacturing for Aerospace Components Using Additive Manufacturing, Net Shape HIP and Investment Casting – within the *Horizon 2020* Framework Programme is gratefully acknowledged.

This research work is also supported by the National Natural Science Foundation of China (Grants 51323008 and 51271213), the National Basic Research Program of China (Grants 2011-CB610402), the National High Technology Research and Development Program of China (Grant 2013-AA031103), the Specialized Research Fund for the Doctoral Program of Higher Education of China (Grant No. 2011-6102110016) and the State Administration of Foreign Experts Affairs of China through the *High-end Experts Recruitment Program*.

References

- Agelet de Saracibar C., Cervera M. and Chiumenti M., On the formulation of coupled thermoplastic problems with phase-change, *Int. Journal of Plasticity*, **15** (1999) 1-34.
- Aggarangsi P., Beuth J., Griffith M., Melt pool size and stress control for laser-based deposition near a free edge. *Proc. solid freeform fab symp.* The University of Texas at Austin, (2003) 196–207.
- Anca A., Fachinotti V., Escobar-Palafox G., Cardona A., Computational modelling of shaped metal deposition. *Int J Numer Methods Eng* **85**(1) (2011) 84–106.
- Birmingham M.J. , McDonald S.D. , Dargusch M.S. , StJohn D.H. , Microstructure of Cast Titanium Alloys, *Materials Forum*, **31** (2007).
- Cervera M., Agelet de Saracibar C. and Chiumenti M., Thermo-mechanical analysis of industrial solidification processes, *Int. Journal for Num. Methods in Engineering*, **46** (1999) 1575-1591.
- Bugeda G., Cervera M., Lombera G., Oñate E., Numerical analysis of stereolithography processes using the finite element method, *Rapid Prototyping Journal*, **1** (2) (1995) , pp. 13-23.

Bugeda G., Cervera M., Lombera G., Numerical prediction of temperature and density distributions in selective laser sintering processes, *Rapid Prototyping Journal*, **5**(1) (1999) 21-26.

Cervera M., Agelet de Saracibar C. and Chiumenti M., COMET: COupled MEchanical and Thermal analysis. Data Input Manual, Version 5.0, Technical report IT-308 (2002), <http://www.cimne.com/comet>.

Chiumenti M., Agelet de Saracibar C. and Cervera M., On the Numerical Modelling of the Thermo-Mechanical Contact for Metal Casting Analysis, *Journal of Heat Transfer*, **130** (2008) 1-10.

Chiumenti M., Cervera M., Salmi A., Agelet de Saracibar C., Dialami N., Matsui K., Finite element modeling of multi-pass welding and shaped metal deposition processes. *Comput Method Appl Mech Eng* **199** (2010), 2343–2359; DOI: 10.1016/j.cma.2010.02.018.

Darmadi D. B., Validating the Accuracy of Heat Source Model via Temperature Histories and Temperature Field in Bead-on-plate Welding, *Int. J. of Eng. & Technology*, **11**(5) (2011) 111505-6868.

Deng D., Murakawa H., Numerical simulation of temperature field and residual stress in multi-pass welds in stainless steel pipe and comparison with experimental measurements, *Computational Materials Science* **37** (2006) 269–277.

Deng D., Murakawa H., Liang W., Numerical simulation of welding distortion in large structures, *Comput. Methods Appl. Mech. Engrg.* **196** (2007) 4613–4627.

Denlinger E., Heigel J., Michaleris P. Residual stress and distortion modelling of electron beam direct manufacturing Ti-6Al-4V. *Proc Inst Mech Eng B:J Eng Manuf.* **11** (2014) <http://dx.doi.org/10.1177/0954405414539494>.

Elmer J. W., Palmer T. A., Babu S.S., Zhang W., and DebRoy T., Phase transformation dynamics during welding of Ti-6Al-4V, *Journal of Applied Physics*, n. 12, **95** (2004), DOI: 10.1063/1.1737476.

Gajapathi S.S., Mitra S. K. and Mendez P. F., Controlling heat transfer in micro electron beam welding using volumetric heating, *International Journal of Heat and Mass Transfer*, **54** (2011) 5545–5553.

GiD: The personal pre and post preprocessor. <http://www.gidhome.com>.

Goldak J., Chakravarti A., Bibby M., A new finite element model for welding heat sources, *Metall. Trans.* **15B** (1984) 299–305.

Heigel J.C., Michaleris P., Reutzel E.W., Thermo-mechanical model development and validation of directed energy deposition additive manufacturing of Ti-6Al-4V, *Additive Manufacturing* **5** (2015) 9–19.

Huang W.D. and Lin X., Research progress in laser solid forming of high - performance metallic components at the state key laboratory of solidification processing of China, *3D Printing and Additive Manufacturing*, **1**(3) (2014) 156–165

- Jendrzejewski R., Sliwinski G., Krawczuk M., Ostachowicz W., Temperature and stress fields induced during laser cladding, *Computer and Structures*, 82(7) (2004) 653–8.
- Jendrzejewski R., Sliwinski G., Investigation of temperature and stress fields in laser cladded coatings. *Appl Surf Sci*, 254(4) (2007) 921–5.
- Kelly S., Kampe S., Microstructural evolution in laser-deposited multi-layer Ti-6Al-4V builds: Part II. Thermal modeling, *Metall. Mater Trans A* 35(6) (2004) 1869–79.
- Labudovic M., Hu D., Kovacevic R., A three dimensional model for direct laser metal powder deposition and rapid prototyping. *J Mater Sci*, 38(1) (2003) 35–49.
- Lacki P. and Adamus K., Numerical simulation of the electron beam welding process, *Computers and Structures*, **89** (2011), 977–985.
- Marimuthu S., Clark D., Allen J., Kamara A., Mativenga P., Li L., Finite element modelling of substrate thermal distortion in direct laser additive manufacture of an aero-engine component. *Proc Inst Mech Eng C: J MechEng Sci* **227**(9) (2013) 1987–99.
- Rahman M., Maurer W., Ernst W., Rauch R. and Enzinger N., Calculation of hardness distribution in the HAZ of micro-alloyed steel, *Weld World*, **58** (2014), 763-770, DOI: 10.1007/s40194-014-0156-5.
- Rosenthal D., Mathematical theory of heat distribution during welding and cutting, *Welding J.* **20** (5) (1941) 220–234.
- Tan H., Chen J., Zhang S.Y., Lin X. and Huang W. D., Process analysis for laser solid forming of thin-wall structure. *International Journal of Machine Tools & Manufacture*, **50**(1) (2010) 1–8.
- Tan H., Chen J., Zhang S.Y., Lin X. and Huang W. D., Estimation of laser solid forming process based on temperature measurement. *Optics and Laser Technology*, **42**(1) (2010) 47–54.
- Tian Y., Wang C., Zhu D. and Zhou Y., Finite element modeling of electron beam welding of a large complex Al alloy structure by parallel computations, *Journal of materials processing technology*, **199** (2008) 41–48.
- Wang L., Felicelli S., Pratt P., Residual stresses in LENS-deposited AISI 410 stainless steel plates. *Mater Sci Eng A: Struct* **496**(1) (2008) 234–41.
- Wei L., Lin X., Wang M. and Huang W.D., Orientation selection of equiaxed dendritic growth by three-dimensional cellular automaton model. *Physica B: Condensed Matter*, **407**(13) (2012) 2471–2475
- Wei L., Lin X., Wang M. and Huang W.D., Cellular automaton simulation of the molten pool of laser solid forming process. *Acta Physica Sinica*, **64**(1) (2015) 018103
- Yang Y.P., Babu S., An integrated model to simulate laser cladding manufacturing process for engine repair applications. *Weld World*, **54**(9–10) (2010) R298–307.

1
2
3
4
5
6
7
8
9
10
11
12
13
14
15
16
17
18
19
20
21
22
23
24
25
26
27
28
29
30
31
32
33
34
35
36
37
38
39
40
41
42
43
44
45
46
47
48
49
50
51
52
53
54
55
56
57
58
59
60

Zhang S.Y., Lin X., Chen J. and Huang W. D., Heat-treated microstructure and mechanical properties of laser solid forming Ti-6Al-4V alloy. *Rare Metals*, **28**(6) (2009) 537-544

Zekovic S., Dwivedi R., Kovacevic R., Thermo-structural finite element analysis of direct laser metal deposited thin-walled structures. *Proc solidfreeform fab symp. The University of Texas at Austin*, (2005) 338-55.